
Article:
Alvarez -Ruiz, DT, Azough, F, Hernandez-Maldonado, D et al. (6 more authors) (2018) Utilising unit-cell twinning operators to reduce lattice thermal conductivity in modular structures: Structure and thermoelectric properties of $Ga_2O_3(ZnO)_9$. Journal of Alloys and Compounds, 762. pp. 892-900. ISSN 0925-8388

https://doi.org/10.1016/j.jallcom.2018.05.260

Utilising unit-cell twinning operators to reduce lattice thermal conductivity in modular structures: structure and thermoelectric properties of $Ga_2O_3(ZnO)_9$

Diana T. Alvarez -Ruiz[1], Feridoon Azough[1],

David Hernandez-Maldonado[2], Demie M. Kepaptsoglou[2], Quentin M. Ramasse[2],

Sarah J. Day[3], Peter Svec[4], Peter Svec Sr.[4], Robert Freer[1,*]

[1] School of Materials, University of Manchester, Manchester, M13 9PL, U.K.

[2] SuperSTEM Laboratory, STFC Daresbury Campus, Daresbury WA4 4AD, U.K.

[3] Diamond Light Source, Harwell Science and Innovation Campus, Oxfordshire, OX11 0DE, UK

[4] Institute of Physics, Slovak Academy of Sciences, Bratislava 845 11, Slovak Republic

[*]corresponding author: Robert.Freer@manchester.ac.uk

ABSTRACT

The $Ga_2O_3(ZnO)_m$ family of homologous compounds have been identified as potential thermoelectric materials, but properties are often limited due to low densification. By use of B_2O_3 as an effective liquid phase sintering aid, high density, high quality ceramic samples of $Ga_2O_3(ZnO)_9$ have been synthesized. The atomic structure and local chemical composition of $Ga_2O_3(ZnO)_9$ have been determined by means of high resolution X-ray diffraction and atomic resolution STEM-HAADF, EDS and EELS measurements. X-ray analysis showed that the compound crystalizes in the *Cmcm* orthorhombic symmetry. Atomically resolved HAADF-STEM images unambiguously showed the presence of nano-sized, wedge-shaped twin boundaries, parallel to the b-axis. These nano-scale structural features were chemically investigated, for the first time, revealing the exact distributions of Zn and Ga; it was found that Ga ions occupy sites at the junction of twin boundaries and inversion boundaries. HAADF-EDS analysis showed that the calcination step has a significant impact on crystal structure homogeneity. By use of a sintering aid and optimization of processing parameters the ceramics achieved a low thermal conductivity of 1.5 to 2.2 W/m.K (for the temperature range 300 to 900 K), a power factor of 40 to 90 $\mu W/K.m^2$, leading to a ZT of 0.06 at 900 K. The work shows a route to exploit nanoscale interface features to reduce the thermal conductivity and thereby enhance the thermoelectric figure of merit in complex thermoelectric materials.

Keywords: Ceramics; oxide materials; thermoelectic materials; solid state reactions; transmission electron microscopy, TEM; $Ga_2O_3(ZnO)_9$;

1. INTRODUCTION

The application of traditional thermoelectric metallic alloys is restricted by several challenges. For instance, alloy sublimation at elevated temperatures limits their reliability and operational range. Meanwhile the low abundance, cost and environmental impact of key constituent elements is driving the search towards more environmental friendly alternatives, such as oxides [1–3], which can operate over broader and more demanding temperature ranges. Selection criteria for candidate materials include the need for both high electrical conductivity and low thermal conductivity. The typical thermoelectric figure of merit (ZT) of oxide materials is lower than that of their alloy counterparts, but the interesting crystal structures exhibited by nano-periodic oxides, make them promising candidates for thermoelectric applications.

Recently, the $Ga_2O_3(ZnO)_m$ homologous compounds [4–9] have attracted attention as potential thermoelectric materials due to the presence of naturally occurring twinned nanostructures, which readily scatter phonons, thereby reducing the thermal conductivity. The first $Ga_2O_3(ZnO)_m$ compounds were synthesised by Nakamura et al. [10]. They proposed a "distorted" wurtzite structure for the solid solution range of $(Ga_2O_3)_x(ZnO)_{1-x}$ ($0 \leq x \leq 0.093$) instead of a layered type structure. Subsequently, Kimizuka et al. [11] reported the formation of $Ga_2O_3(ZnO)_m$ homologous compounds with an orthorhombic *Cmcm* space group. It was suggested that Ga atoms can only occupy tetrahedral sites in $Ga_2O_3(ZnO)_m$ [11], and thus why they do not crystallise isostructurally with $LuFe_3(ZnO)_m$ [12]. Later, Li et al. [13] examined $Ga_2O_3(ZnO)_m$ (m=9 and 13) by high resolution transmission electron microscopy and image simulation techniques and proposed a twinned structure comprising stacks of Ga-O and (m + 1) Ga/Zn-O layers along the c-axis, with a zigzag arrangement of anions and cations with the non-centrosymmetric $Cmc2_1$ space group for m = 9. Michiue and Kimizuka [5] introduced a

superspace formalism to describe the structure of the homologous series $Ga_2O_3(ZnO)_m$, treating them as compositely-modulated structures, consisting of two subsystems. They suggested that the distribution of Ga and Zn in $Ga_2O_3(ZnO)_m$ resembles the arrangement of Zn cations in the Wurtzite structure of ZnO, and the arrangement of O anions resembles the framework made by O anions in the Wurtzite structure.

The exact structures of the $Ga_2O_3(ZnO)_9$ homologous compound and specifically the occupancy of the Zn and Ga lattice sites are not well established [4–8,14]. This is, in part, due to analytical limitations of the radiation techniques, arising from the close proximity of the atomic numbers of Zn and Ga, making the exact determination of the site occupancy of Ga and Zn in the twin boundaries and the accompanying inversion boundaries very difficult. The presence of Ga-induced, non-periodic twin boundaries and inversion boundaries on the $\{01\bar{1}3\}$ planes of ZnO has been reported [9,15], showing segregation of Ga in the twin and inversion boundaries.

The twinned crystal structure of the $Ga_2O_3(ZnO)_m$ compounds tends to encourage anisotropic, plate-like grains which are difficult to densify in ceramic form. Michiue et al.[6] synthesised polycrystalline $Ga_2O_3(ZnO)_9$ at 1723 K and achieved a density of only 57% theoretical. By the use of Cold Isostatic Pressing (CIP) the density was increased to 73%, which is still modest by the standards of most functional ceramics. However, the electrical conductivity of the low density sample was as high as 13 S/cm, which was comparable with that exhibited by the more expensive indium analogue, $In_2O_3(ZnO)_9$ [16]. In view of the encouraging electrical conductivity reported for the very low density $Ga_2O_3(ZnO)_9$ ceramics [6], and the fact that the layered structure materials are expected to have low thermal conductivity [17], the $Ga_2O_3(ZnO)_9$ ceramics should exhibit enhanced and potentially useful thermoelectric properties if the problem of very low density can be addressed.

In this study, we synthesised and investigated the crystal structure and thermoelectric properties of ceramic $Ga_2O_3(ZnO)_9$. We selected this member of the homologous series because of the promising thermoelectric properties [6], although recognising that limited structural data had been reported [5,6]. To enhance density we employed B_2O_3 as a sintering aid to both reduce the processing temperatures and increase sample quality [18].

In view of the uncertainties concerning structural details of $Ga_2O_3(ZnO)_9$ and the fact that nano-scale features in the microstructure have a significant impact on thermoelectric properties [6,9,19], we employed X-ray diffraction and electron microscopy techniques. The exact crystal structure of $Ga_2O_3(ZnO)_9$ was determined by combined high resolution X-ray diffraction and atomic resolution analytical Scanning Transmission Electron Microscopy (STEM) techniques; namely High and Medium Angle Annular Dark Field imaging (HAADF and MAADF, respectively), Energy Dispersive X-ray spectroscopy (STEM-EDS) and Electron Energy Loss spectroscopy (STEM-EELS). The atomically resolved HAADF- and MAADF-STEM images unambiguously showed the presence of nano-sized features; these structural features were chemically investigated, for the first time, revealing the exact distribution Zn and Ga in $Ga_2O_3(ZnO)_9$.

2. MATERIALS AND METHODS

$Ga_2O_3(ZnO)_9$, hereafter identified as Z_9GO, ceramics were prepared by the conventional solid-state reaction technique. The starting raw materials, reagent-grade ZnO and Ga_2O_3 were mixed in molar ratios 9:1 and vibratory milled for 24 h. After a series of trial experiments the mixed powders were calcined at 1473 for 4 h. The calcined powders were milled again for 24 h; during this second milling stage 0.2 wt% of B_2O_3 was added. The dried powders were uniaxially

pressed in a 20 mm die at ~25 MPa and then sintered in air for 2, 4 and 12 h at 1673 K, under powder bed of the same composition; samples are denoted as 2H, 4H and 12H respectively. One set of samples were sintered at 1673 K for 4 h without being calcined; these are denoted as NC.

The microstructures of the polished surfaces of the samples were analysed using Philips® XL30 (FEG)-SEM HKL® microscope equipped with an energy-dispersive X-ray (EDX) detector.

Initial X-ray diffraction studies and phase identification of the calcined powders were carried out using a Philip PANalytical X'Pert Pro® diffractometer with Cu Kα radiation, for 2θ ranging from 10° to 100° in steps of 0.017. For Synchrotron Radiation X-ray Powder Diffraction (SR-XPD) study, the sintered pellets were ground and mounted in a 0.5 mm borosilicate glass capillary, which was irradiated with the I11 beamline (λ = 0.825625(10) Å and E=15 keV) at the Diamond Light Source over the 0-100° 2θ range. Rietveld full-profile refinement [20] was undertaken using Topas 5.0 [21].

For the Transmission Electron Microscope (TEM) observations, samples were conventionally prepared by crushing in a pestle and mortar and drop cast onto lacey carbon support grids. The specimens were initially investigated using selected area electron diffraction (SAED) and high-resolution transmission electron microscopy (HRTEM) techniques using an FEI FEG-TEM (Tecnai G2 F30) operating at 300 kV.

Atomic-resolution structural characterization was carried out using a Nion UltraSTEM aberration-corrected dedicated STEM equipped with a Gatan Enfina electron energy loss spectrometer. This microscope was operated at 100 kV acceleration voltage and the probe-forming optics were adjusted to form a 0.9 Å electron probe with a convergence of 31 mrad and beam current of approximately 50 pA. The HAADF detector inner and outer semi-angles were calibrated at 82-189 mrad, while for all electron energy loss spectroscopy (EELS) data presented

here the collection semi-angle (spectrometer acceptance angle) was 36 mrad. EELS spectrum images (EELS SI) were acquired by rastering serially across a defined area of the specimen, recording an EEL spectrum at each position. EELS SI data for chemical mapping were de-noised by Principal Component Analysis using the MSA Cime- EPFL plugin [22] for Digital Micrograph. EELS chemical maps, namely Zn $L_{2,3}$ were subsequently produced by integrating pixel-by-pixel the intensity edges) over a fixed energy window of 40 eV above the edge onset, after subtraction of the decaying background using a standard power law fitting function.

Atomic-resolution Energy-dispersive X-ray spectroscopy (EDS) was performed in an FEI Themis Electron Microscope operated in STEM mode at 200 kV. EDS acquisition was carried out using a Super-X detector system (ChemiSTEM technology). EDS spectrum images were acquired by continuously rastering serially across a defined area of the specimen, recording cumulative EDS spectra at each position. EDS chemical maps were produced by integrating the intensity of the Zn K_α and Ga K_α absorption peaks, respectively.

The Electrical Conductivity of the samples was measured using the four-probe method, and their Seebeck coefficient was measured using the differential method. Both properties were measured simultaneously from room temperature to 873 K in an ULVAC® ZEM-3® using 2x2x12mm samples. The thermal conductivity (κ) was determined from the thermal diffusivity (α), heat capacity (C_p) and density (ρ), using the relationship:

$$\kappa = \alpha C_p \rho \qquad (1)$$

The thermal diffusivity of the samples was measured using the Laser Flash Technique (LFT) in an Argon atmosphere at atmospheric pressure using the NETZCH® LFA 427®. The heat capacity was measured by the Differential Scanning Calorimeter Netzsch® STA 449 C® in a reducing atmosphere. Density was determined by the Archimedes method.

3. RESULTS AND DISCUSSION

3.1.Optimization of the Microstructure

Following trial experiments, a calcination temperature of 1473 K was adopted. It enabled development of a significant fraction of the target phase $Ga_2O_3(ZnO)_9$ (denoted as Z_9GO), without excessive particle growth, although both ZnO and $ZnGa_2O_4$, were present in the powder (Figure 1a). A range of sintering temperatures were explored. At and below 1623 K, the products were of low density (less than 90% theoretical) and still contained the $ZnGa_2O_4$ secondary phase. Temperatures above 1673 K led to microcracks and unnecessary volatilisation of ZnO. Samples sintered at 1673 K for 2 to 12 hours (denoted as 2H to 12H etc) were single-phase (Figure 1b), crack-free, high density and typically 90% theoretical, independent of the sintering time. Figure 2 shows typical Back Scattered Electron (BSE) SEM micrographs of samples sintered for 2 and 4 hours. All the grains exhibit plate-like morphologies with an average grain size ~ 20 μm (Figure 2); for longer sintering times there was a slight increase in grain size. The resulting samples (sintered at 1673 K for 2 to 12 hours) were subjected for further crystal structure and thermoelectric property analysis.

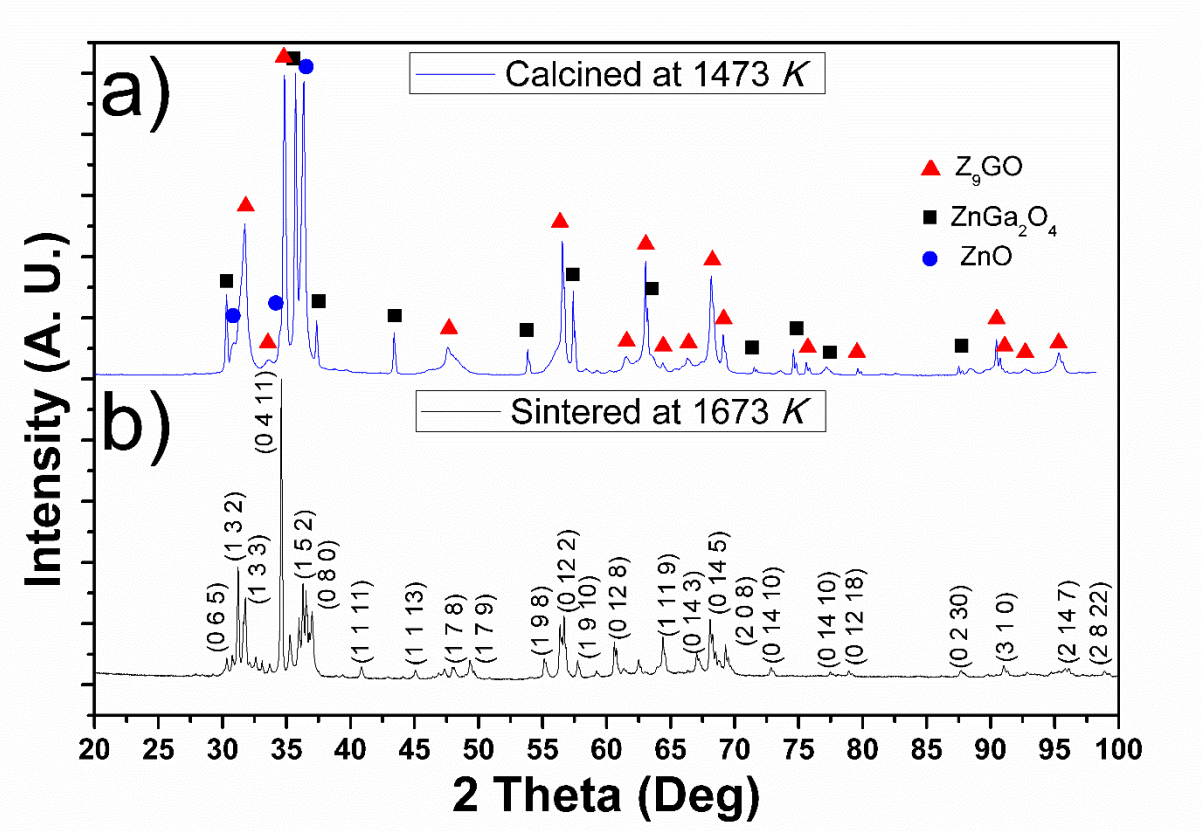

Figure 1. XRD spectra for the Z_9GO powders (a) calcined for 4 hours at 1473 and then (b) sintered at 1673 K (sample 4H).

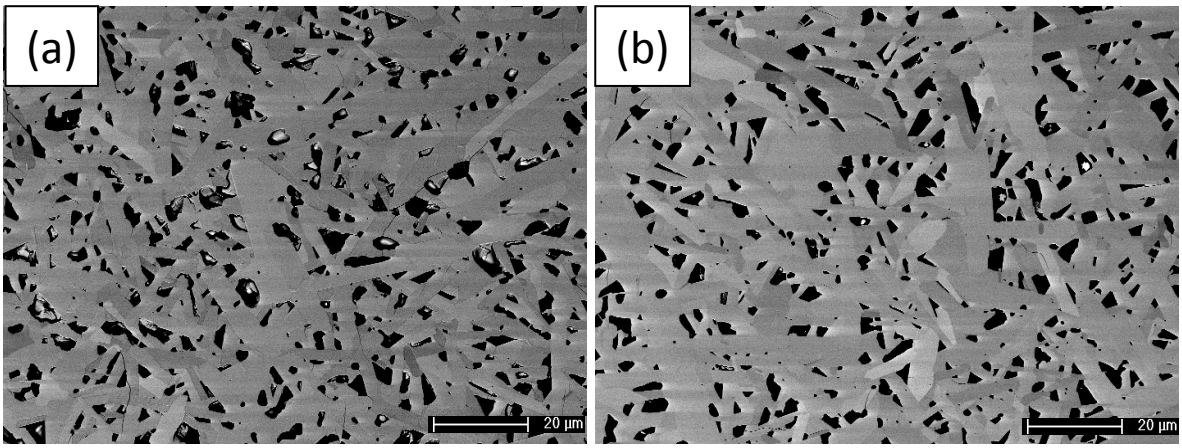

Figure 2. BSE-SEM images of ceramic Z_9GO: (a) 2H, and (b) 4H.

3.2.Atomic scale characterization

As mentioned earlier, the refinement the crystal structure, and explicitly the relative occupancy of the lattice sites in Ga and Zn, is particularly challenging solely from XRD data. In order to better inform the structure refinement, atomic scale structural and chemical information is needed. For this we turn to local probe techniques and more specifically electron microscopy. High precision STEM imaging and analysis as well as atomically resolved chemical mapping were performed in order to obtain the relative occupancy of atomic columns in Zn and Ga.

Figures 3a and 3b show HAADF STEM images (non-rigid reconstructed from stacks of ~30 frames) of the sample with the highest figure of merit, 4H-Z_9GO, acquired with the incident electron beam parallel to the [100] direction; the images reveal a head to head type twinned nanostructure, with a wedge apex angle of about ~63.37° (marked in Figure 3b). The boundaries of the twins, labelled as TB in Figure 3b, are parallel to the *b*- axis of the crystal structure. The deduced width of the twins from the lattice images is about 33 Å in agreement with HRTEM (see Figure S1 in the in the supplementary information provided). The well-ordered nano-TB are marked with parallel white lines (Figure 3b). The $m + 1 = 10$ atomic columns in between the wedge shaped nano-TB boundaries are observed, as reported in previous HRTEM studies [13]. The width of the nano-twins is uniform throughout the region screened in Figure 3, corresponding to $m + 1 = 10$ atomic columns. The stacking sequence in the modular structure of the $Ga_2O_3(ZnO)_m$ compounds must be described considering both, the twin and inversion boundaries as structure building operators [4,14,15][9]. Recently Guilmeau et al. [9] showed that in HAADF images of heavily twinned ZnO doped with 4mole% Ga, the twin widths were generally large, about 100 nm, and the inversion boundaries appeared as dark bands mid-way between the twin boundaries. However, in the present samples there is no variation in the

contrast of the HAADF image of sample 4H (Figure 3a,b). This is possibly because of the smaller width of twin in this sample.

In contrast to the 4H-Z_9GO sample, the HAADF–MAADF-STEM images of the corresponding NC-Z_9GO sample (prepared without calcination processing stage, Figure 3c and d), show a non-periodic arrangement of the nano-TB with evidence of the presence of inversion boundaries (white bands in the MAADF image). This non-periodic arrangement of the nano-TB boundaries cannot be expressed as $Ga_2O_3(ZnO)_m$ or $(Ga_2O_3)_2(ZnO)_{2m+1}$ homologous compounds.

The distribution of Zn and Ga in the Z_9GO structure was investigated by atomically resolved STEM-EDS (Figure 4). The atomically resolved STEM-EDS maps shown in Figure 4 reveal the prevalence of Ga (and corresponding Zn depletion) at the TB, more specifically by the darker atomic columns in the HAADF images of both the 4H- and NC-Z_9GO samples (Figure 4 c and g, respectively). The Ga partially-occupied TB observed in the HAADF-EDS maps (Figure 4) shows that Ga and Zn occupy the alternate lattice sites in the twin boundaries. The distribution of Zn in the NC sample was also confirmed by atomic resolution EELS mapping (Figure 3 in SI). This finding is in good agreement with the predictions of Barf et al. [15], based on their low-resolution EELS study, and the Guilmeau et al. [9] HAADF-STEM-EDS study of twin boundaries of Ga doped ZnO. It should be noted that in the Guilmeau et al study [9], the Ga EDS signal was not clearly resolved. However, based on the Zn deficiency in the EDS map at the TBs it was concluded [9] that the TBs should be rich in Ga. The experimental observations by Barf et al. [15] and Guilmeau et al. [9] were supported by the theoretical calculations [14] for a low end member of the homologous series (Z_6GO); it was predicted that twin boundaries on the $\{01\bar{1}3\}$ planes of ZnO would be half occupied by Ga, and would have the polar c −axis of the ZnO pointing towards the twin boundary (head to head configuration) [15]. Furthermore, Ga enriched

bands (depleted in Zn) can be observed parallel and in between the TBs (Figure 4). These Ga rich boundaries can be inferred as inversion boundaries. The formation of Ga containing inversion boundaries in between the nano-TB boundaries has been proposed as structure-building-operators associated with inversion of the orientation of the ZnO teterahedra [15]. Figure 4 confirms past experimental prediction and calculations, showing Ga rich inversion boundaries halfway between the twin boundaries corresponding to Ga agglomerations reversing the polarity of the ZnO c −axis.

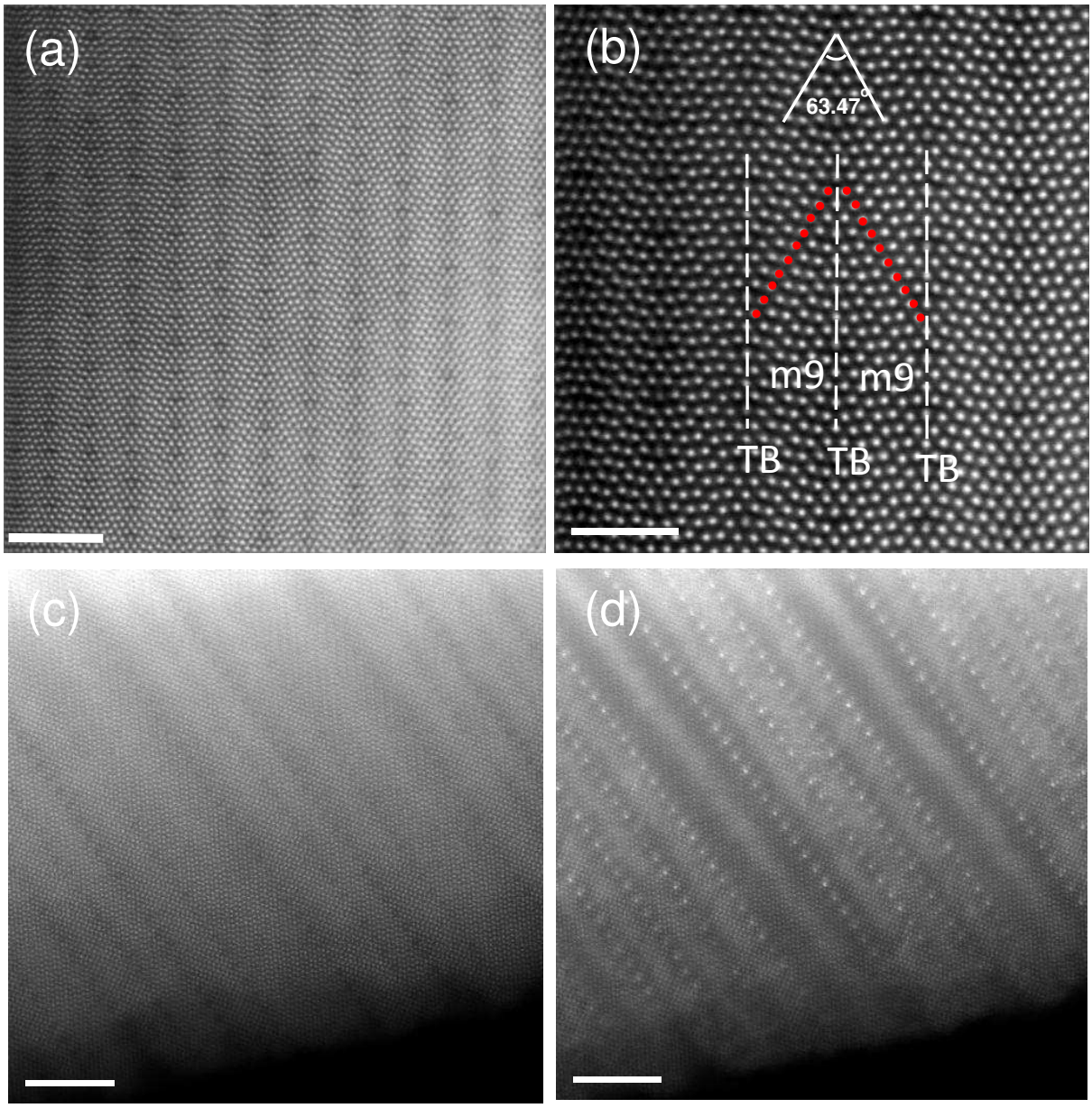

Figure 3. HAADF – MAADF STEM images acquired along the [100] zone axis of Z_9GO samples: (a) and (b) are HAADF images for 4H sample; (c) and (d) are HAADF and MAADF images respectively for the NC sample. The twin boundaries (TB) of the $Ga_2O_3(ZnO)_9$ structure are marked in (b).

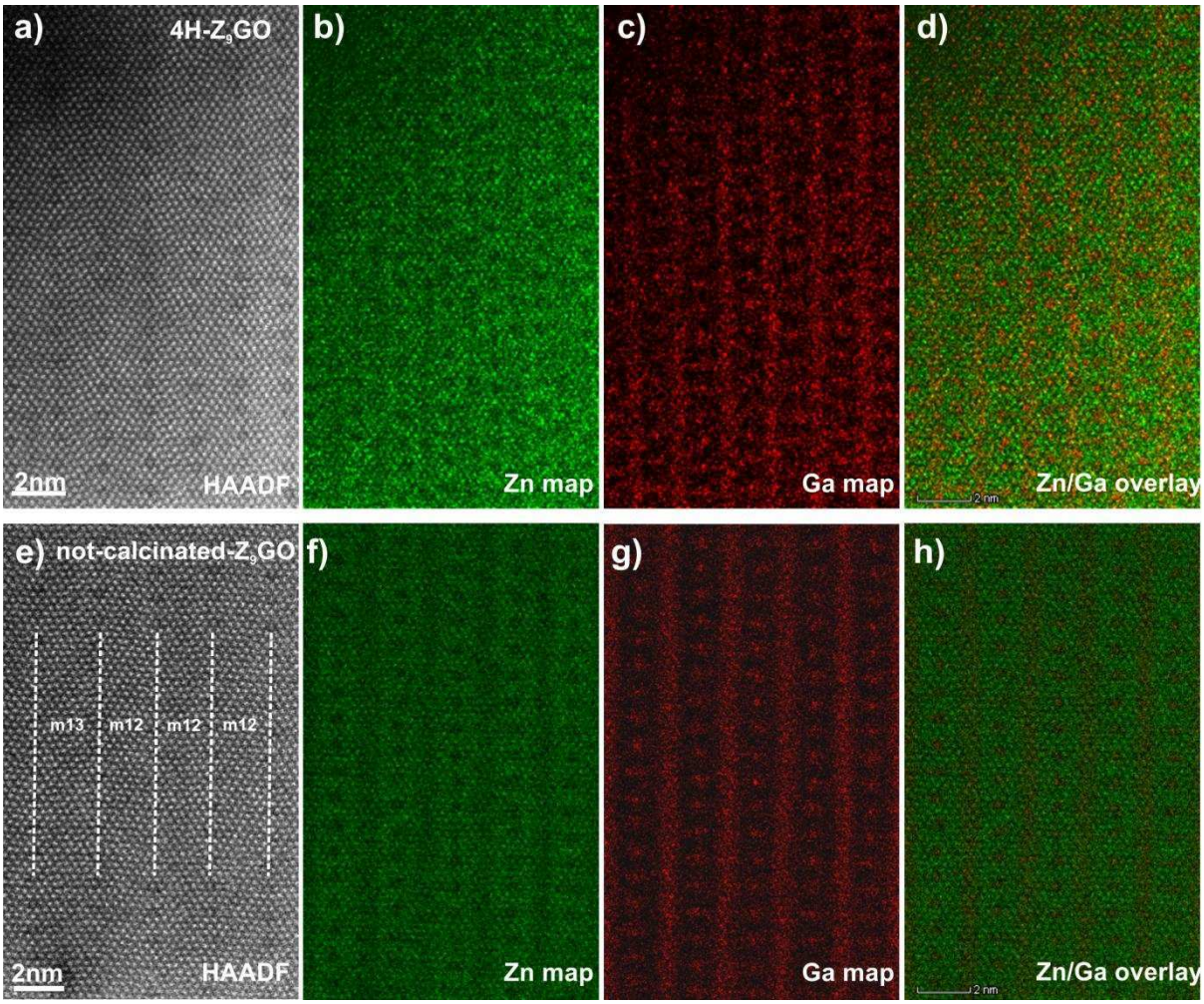

Figure 4. (a),(e) HAADF STEM images and (b-d), (f-h) atomically resolved EDS maps of the 4H and NC- Z_9GO compounds respectively, showing the prevalence of Ga in TB and IB.

HAADF STEM imaging and STEM-EDS mapping therefore clearly show that the calcination process helped to homogenize the Zn and Ga distribution throughout the structure of the homologous compounds, achieving a more periodic distribution of the nanotwin and inversion boundaries after a calcination stage. Although, in the NC-Z_9GO sample the number of Ga/Zn-O layers is not even, the distribution of Ga atoms is preserved (Figure 4).

3.3.XRD refinement

For the structural refinement, the crystal structure parameters given in the $(3 + 1)$ dimensions using the superspace formalism presented by Michiue et al. [5] (and converted to three dimensional format by the same group [6]) was used as a starting point to further improve the structural model. In the prosed model [6], Zn has been considered as the main element for all the lattice sites throughout of the entire crystal structure. This is the same for the distribution of Ga but with much lower content compared to the Zn to maintain the stoichiometry. However, our HAADF-STEM-EDS data showed very different site occupancies specifically for both Ga and Zn. Therefore, the elemental distribution data from both HAADF-STEM imaging and atomic resolution EDS mapping was used for site occupancies of Zn and Ga in the input structural file for Rietveld refinement of the synchrotron X-ray diffraction data.

The modified structural parameters (coordinates and site occupancies for Ga) based on electron microscopy observations from the sample 4H-Z_9GO were used to perform a Rietveld refinement on the SR-XPD data, using the suggested *Cmcm* space group [6]. Cell dimensions, lattice parameters, peak shape, site occupancies, thermal displacement parameters and background were refined; the final lattice parameters obtained through the Rietveld refinement, are shown in Table 1, along with the goodness of fit (GOF) and the R indexes (R_{wp} and R_p). The refined coordinates for Zn, Ga and O and their site occupancies are listed in Table S1. All the reflections are fully indexed with the optimized crystal structure obtained. The refined lattice parameters were not significantly affected by the sintering time; a slight increase in the unit cell volume is observed for the 4H sample due to slightly higher values for unit cell dimensions, *a* and *b*. The result of the Rietveld refinement of the full spectrum for 4H –Z_9GO sample is shown in Figure 5.

Table 1. Structural parameters and R-factors obtained after Rietveld refinement.

Sample Label / Parameter	2H	4H	12H
a (Å)	3.25226(6)	3.25302(6)	3.25240(6)
b (Å)	19.7124(4)	19.7142(4)	19.7111(4)
c (Å)	33.6306(6)	33.6355(6)	33.6315(7)
R_{wp}	3.17	3.15	3.13
R_p	2.18	2.16	2.13
GOF	4.82	4.68	4.68

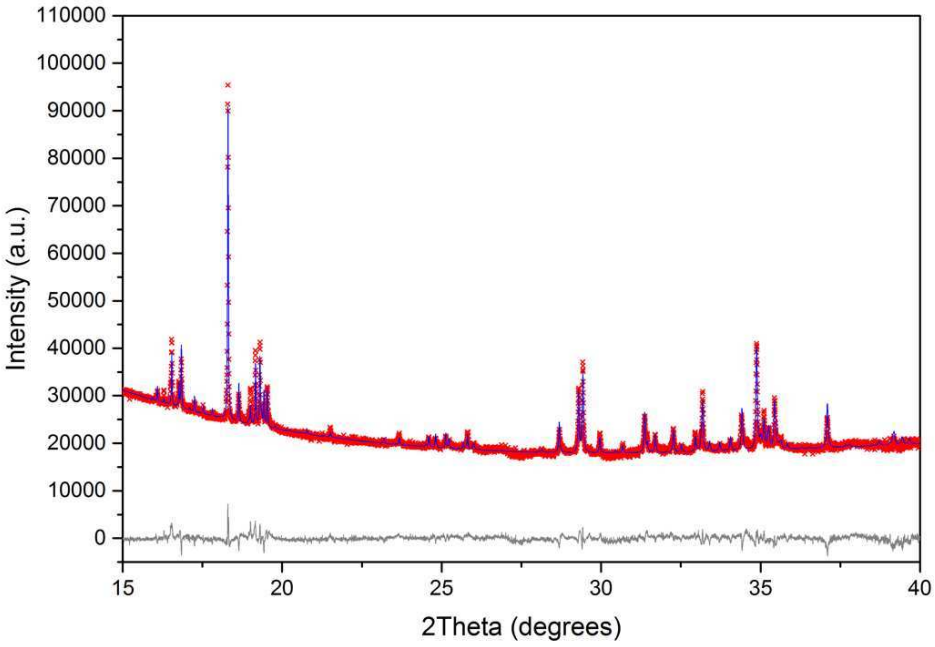

Figure 5. Final Rietveld refinement of data for the 4H-Z_9GO sample using the proposed crystal structure for Z_9GO. The red crosses correspond to the experimental data, the blue line to the calculated pattern, and the grey line the difference between experimental and calculated data.

The resulting crystal structure from the Rietveld refinement of sample 4H- Z_9GO is shown in Figure 6a – alongside a corresponding HAADF STEM image. The purple bipyramids in Figure 6a are occupied by Ga; the positions of the twin and inversion boundaries identified are marked by black arrows. In the twin boundaries Ga and Zn occupy the lattice sites alternatively along the b-direction (Figure 6a); Ga is coordinated with 5 oxygen atoms inside a square pyramid and Zn is located within tetrahedron coordinated with 4 oxygen atoms. In this structure, the occupancy of Ga-O and Zn-O at the twin boundaries is the same the model proposed by Barf et al. [15] for Ga doped Zinc oxide. The superimposed [100] projection of the final crystal structure on the [100] HAADF image is shown in Figure 6b.

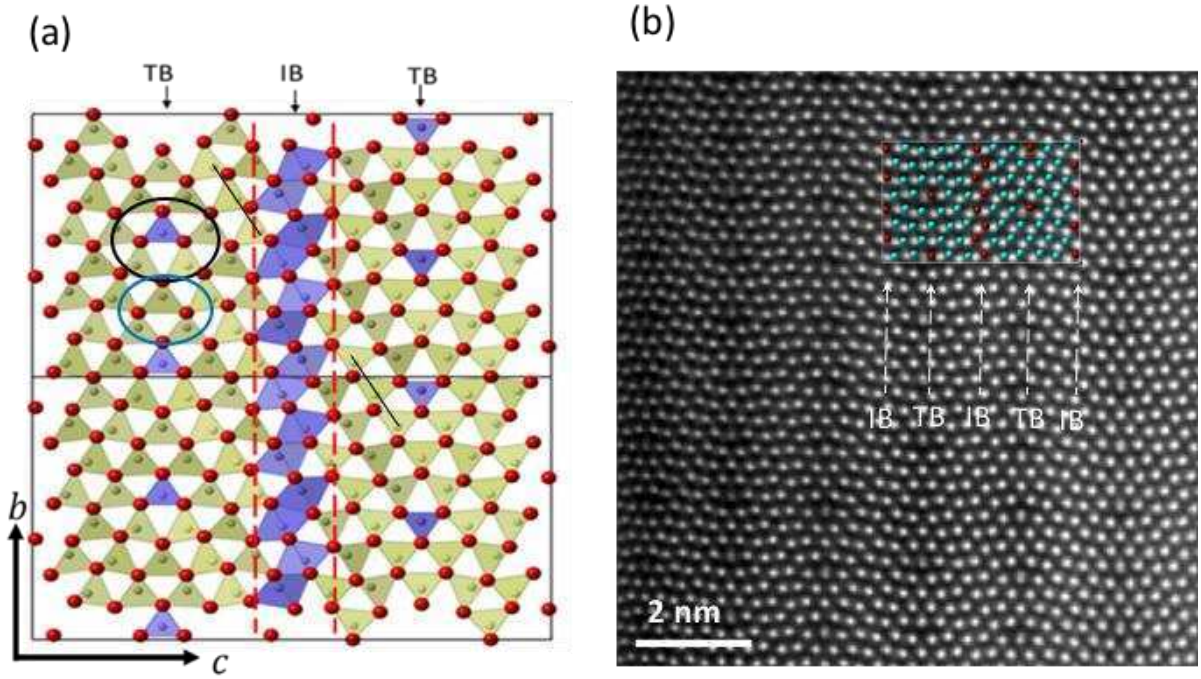

Figure 6. (a), [100] Schematic structural representation of the Z_9GO compound; the position of Ga and its oxygen environment is shown inside black ellipsoid. The position of Zn and its oxygen environment is shown inside blue ellipsoid. An example of tail to tail type inversion of

Zn-O tetrahedral on the either side of IB is shown by black lines. (b) The superimposed [100] projection of the final crystal structure on the [100] HAADF image.

3.4.Thermoelectric Properties

The thermoelectric properties of the Z_9GO compounds are presented in Figure 7. All the samples show n-type behavior, with high Seebeck coefficients that increase with increasing temperature (Figure 7a). The Seebeck coefficients for sample 4H are in the range of -210 and -300 μV/K, and across all samples they are as high as -340 μV/K. In comparison with other homologous compounds, these Seebeck coefficients are at least comparable with or higher (at high temperatures) than most other materials, including the much more expensive indium analogue $In_2O_3(ZnO)_9$ [16,23-25].

All the samples show semiconductor behaviour from room temperature up to 600 K, then metal-like behaviour at higher temperatures (Figure 7b). However, the total variation in electrical conductivity across the full temperature range is modest (~10%). This consistency in electrical conductivity has been noted previously for ZnO ceramics heavily doped with Ga, and was attributed to tunnelling effects induced by superlattice interfaces which limit the electrical conductivity of Ga-ZnO materials [26]. Among the samples investigated, the sample sintered for 4 h (4H-Z_9GO) exhibits the highest electrical conductivity (in the range of 9.5 to 10.5 S/cm), being slightly higher than that for other calcined and the one non-calcined sample. The reason for slightly increased electrical conductivity of sample 4H is not known. However, this increase is consistent with the reduction of Seebeck coefficient of sample 4H compared to the Seebeck coefficients for other samples (Figure 7a). It is noted that the electrical conductivities of the

samples in this study with 90% theoretical density are in the same range as those reported by Michiue et al [6] which had much lower densities (70% theoretical). Very different processing conditions were used in the two studies; higher sintering temperatures and longer times by Michiue et al [6] along with an 'open' sintering atmosphere. The use of B_2O_3 in the present study was critical for achieving high densities, but its ultimate presence in the grain boundaries may have had a deleterious effect on electrical conductivity.

All the samples showed very low thermal conductivity of 2.3 to 1.5 W/K.m (Figure 7c). These values are the lowest reported for homologous compounds based on ZnO heavily doped with Ga[9] and Indium analogues [16,23]. Commonly, all the samples show limited variation in thermal conductivity with temperature (Figure 7c), this being more pronounced for 4H-Z_9GO. The contribution of lattice thermal conductivity (κ_l) to total thermal conductivity was calculated by assuming a Wiedemann-Franz relationship and a constant Lorentz number, ($L_0 = \pi^2 k_B^2/3e^2 = 2.44 \times 10^{-8} W\Omega K^{-2}$). Data for the two components are presented in Figure S3. It is clear that lattice thermal conductivity dominates, being two orders of magnitude larger than the electronic component. This suggests that the total thermal conductivity is mainly controlled by the complex crystal structure exhibited by these homologous compounds and the low thermal conductivity is intimately linked to the range of nano-scale features acting as phonon scattering centers. In particular we propose that the following factors control the thermal conductivity response of Z_9GO homologous compounds: (i) presence of twinned crystal structures; (ii) presence of inversion boundaries; (iii) alternating sequence of occupancy for Ga and Zn with different oxygen coordination in the TB boundaries along the b-direction; (iv) segregation of the Ga in the IBs having different oxygen coordination compared with oxygen coordinated Zn which occupy all the lattice sites between TB and IB boundaries. The low thermal conductivity of the Z_9GO

compounds (Figure 7c) clearly demonstrates the importance and benefit of optimising the processing conditions. There is a dramatic 25 % reduction in thermal conductivity between samples which were not calcined and those which were calcined. This almost certainly reflects the increased homogeneity of microstructure in the samples subjected to a two stage heat treatment.

Finally, the thermoelectric figure of merit (ZT) data for the samples is presented in Figure 7d. As anticipated, the ZT values for 4H-Z_9GO samples are highest while those for NC-Z_9GO samples are the lowest, reflecting the significant differences between their electrical conductivity and thermal conductivity values (Figure 7 a, c). The figure of merit of the NC-Z_9GO sample was effectively doubled by the calcination step, both homogenizing the bulk microstructure and homogenizing the width of the nano-twinned region, thereby lowering the thermal conductivity. Thus, the samples with the most promising thermoelectric properties are those calcined prior to sintering for 4 h at 1673 K, giving densities of 90% theoretical; in the optimised samples, a power factor of 90 $\mu W/K.m^2$ was obtained at 900 K leading to ZT of 0.06 at 900 K.

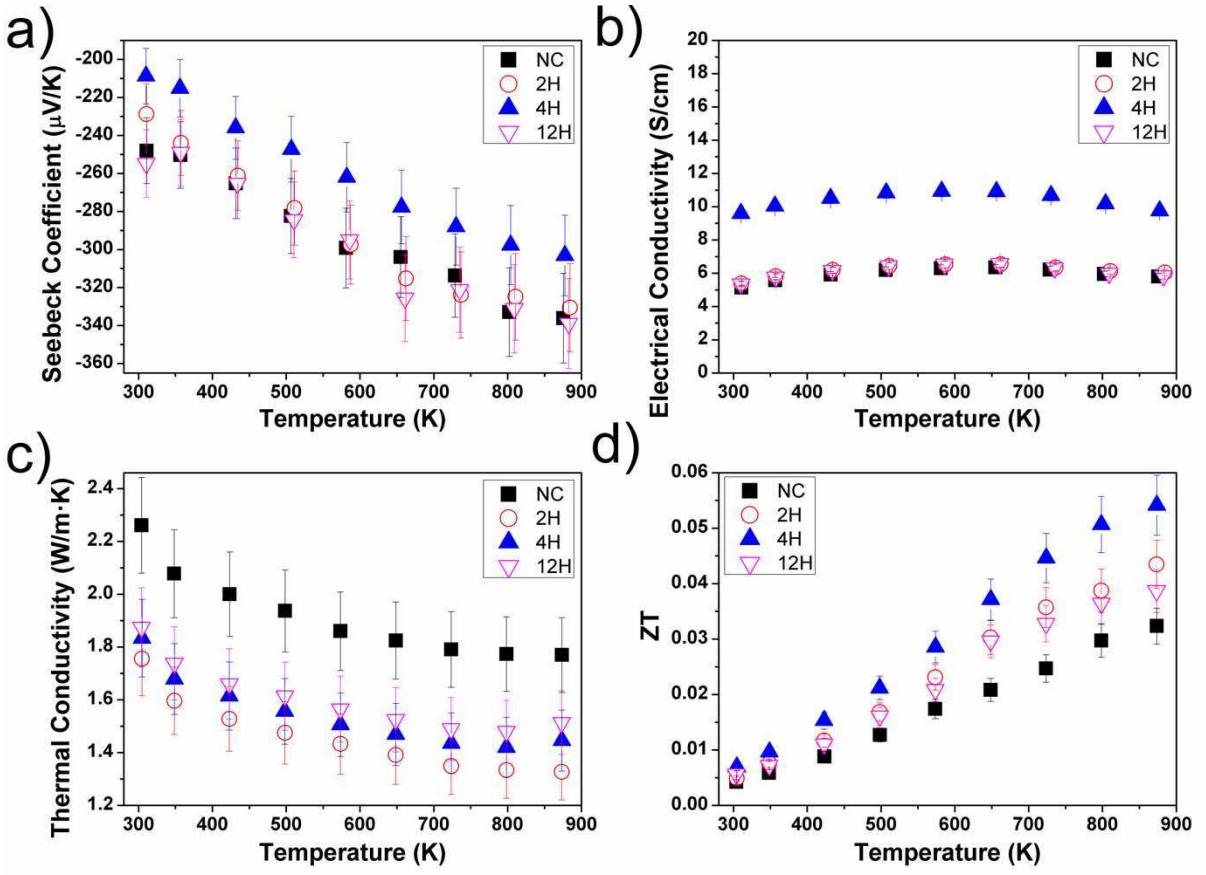

Figure 7. Thermoelectric properties of 0.2 wt% B_2O_3 doped Z_9GO samples (NC, 2H, 4H and 12H): (a) Seebeck coefficient, (b) electrical conductivity, (c) thermal conductivity, (d) thermoelectric figure of merit.

To understand the wider compositional dependence of the thermoelectric properties of the $Ga_2O_3(ZnO)_m$ compounds we have combined our data with the recent results of Guilmeau et al [9]. The relationships can be better revealed by using $Zn_{1-x}Ga_xO_{1+x/2}$ description for the homologous compounds (Figure 8). Samples reported by Guilmeau et al [9] cover low values of x from x = 0.005 to x = 0.04; our samples are equivalent to x = 0.18.

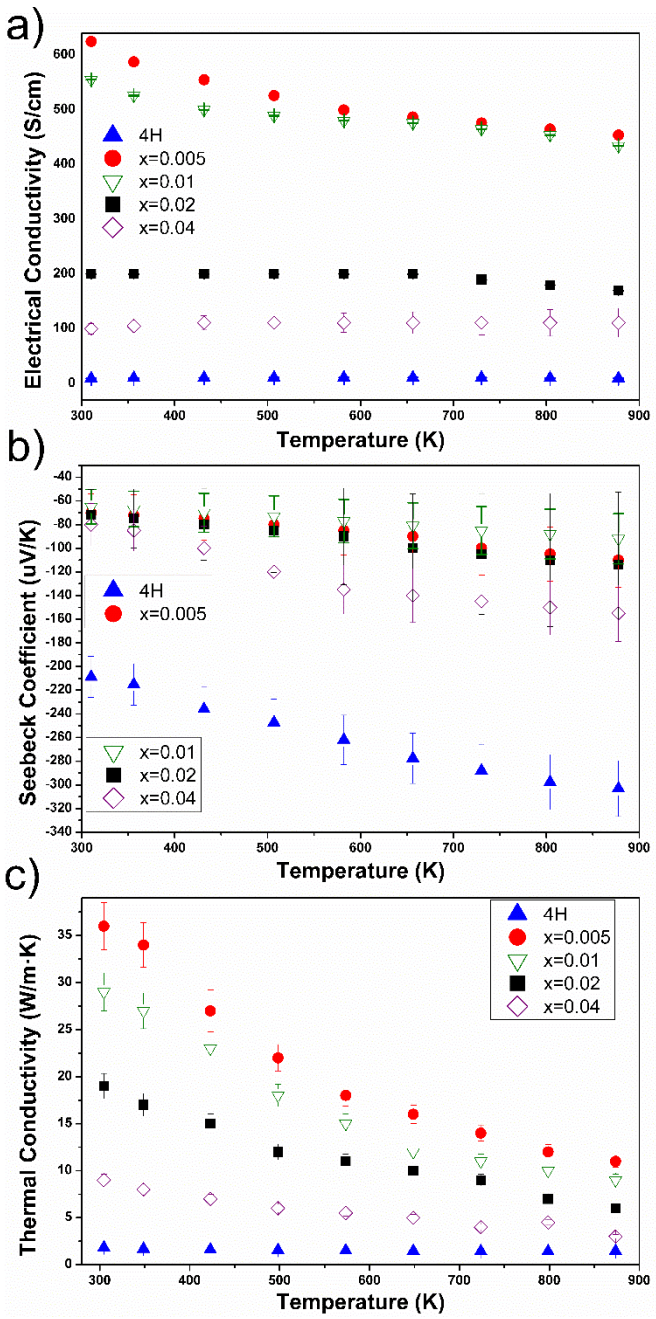

Figure 8. Thermoelectric properties of homologous compounds $Zn_{1-x}Ga_xO_{1+x/2}$ as a function of composition and temperature: (a) electrical conductivity, (b) Seebeck coefficients, and (c) thermal conductivity. Data for samples $0.005 < x \leq 0.04$ taken from Guilmeau et al. [9]; data labelled 4H (equivalent to x = 0.18) from this study.

The collected data in Figure 8 shows that increasing the level of Ga significantly increases the Seebeck coefficients but dramatically reduces electrical conductivity and thermal conductivity. The net reduction in electrical conductivity with increasing Ga content is ascribed to a reduction in carrier concentration and mobility [8,9] as a result of the formation of Ga-rich twin boundaries and inversion boundaries and an increased density of planar defects. The increasingly resistive nature of the samples is accompanied, as expected, by a rapid beneficial increase in Seebeck coefficients. As the homologous series $Ga_2O_3(ZnO)_m$ moves to the lower values of m, such as m = 9 for $Ga_2O_3(ZnO)_9$, not only is there an increase in the number and density of planar defects, but there is also a reduction in the width of the twin domains. Together these lead to the exceptionally low thermal conductivities of ~1.5 W/K.m recorded for $Ga_2O_3(ZnO)_9$ (Figures 7 and 8); such values are very low for any oxide thermoelectric. Whilst the high Seebeck coefficients and low thermal conductivity for $Ga_2O_3(ZnO)_9$ are desirable, the low electrical conductivity limits the thermoelectric figure of merit to ~0.055 at 900 K, which is only marginally lower than the value of 0.065 (at 900 K) reported for $Zn_{1-x}Ga_xO_{1+x/2}$ with x = 0.04 by Guilmeau et al. [9]. Intrinsically, these homologous series compounds are not yet suitable in their own right as viable thermoelectric materials, but understanding and exploiting the nanostructured planar defects in other complex-structured materials could be very valuable.

To summarize, we have confirmed that boron oxide is effective in aiding the synthesis of dense, high quality samples of $Ga_2O_3(ZnO)_9$ as the first essential requirement for further improvement of the properties through control of the processing parameters. Following optimization of the processing parameters, the overall figure of merit sample was doubled by including calcination step to homogenize the width of the nano-twinned region, as confirmed by atomic resolution imaging.

We have shown, for the first time, the existence of the inversion domain boundaries in Z_9GO. Moreover, we have determined the chemistry and cation-oxygen environment for this material. Our data shows that the crystal structure of Z_9GO contains various atomic and nano scale features, namely Ga-O pyramids and Zn-O tetrahedrons at the twin boundaries, Ga-O bipyramids at the inversion boundaries and inverted Zn-O tetrahedrons either side of the inversion boundaries. Consequently, these act as phonon scattering centers promoting very low thermal conductivity for Z_9GO, with the values being the lowest reported so far for any dense homologous ceramic. However, since the samples have been sintered in air, they possess low electrical conductivity, which could be further improved through donor doping. In addition, the thermal conductivity could be further reduced by changing the width between each V-shaped interface when the value of m is modified. Texturing in conjunction with optimized m and doping should be also considered for overall improvement of thermoelectric response, since the ZT value of the textured Indium analogue is very much higher than that of the normally-processed (randomly grain distributed) samples (0.08 compared with 0.30 at 1100 K [17].

4. CONCLUSIONS

High quality Z_9GO ceramics were prepared by liquid phase sintering through the addition of 0.2 wt% of B_2O_3 to the starting materials. The crystal structure was unambiguously resolved by employing a combination of synchrotron radiation and atomic resolution electron microscopy. The Z_9GO crystallizes in an orthorhombic symmetry with $a_0 = 3.2$, $b_0 = 19.67$ and $c_0 = 33.5$ Å in the *Cmcm* space group. The crystal structure contains two types of planar interfaces; (i) head to head twin boundaries and (ii) and tail to tail inversion boundaries. Ga ions occupy the lattice sites at the interface of twin boundaries and inversion boundaries. As a result, Z_9GO

exhibits very low thermal conductivity. The contribution of the low thermal conductivity to the figure of merit, is the main factor increasing the *ZT* at high temperatures. The thermoelectric properties of the Z_9GO compounds are comparable with most expensive and extensively studied $In_2O_3(ZnO)_m$ homologous compounds. The overall thermoelectric response of the Z_9GO and related compounds is still modest. There is scope for improvement through a combination of suitable doping, further inclusion of nano-defects and use of alternative synthesis routes. However, it is clear that the development and presence of natural nanoscale interface features can dramatically reduce thermal conductivity. Exploiting such features by engineering the nanostructures of complex thermoelectric materials could lead to significant improvement in thermoelectric performance.

ACKNOWLEDGMENTS

The authors are grateful to the EPSRC for the provision of funding for this work (EP/H043462, EP/I036230/1, EP/L014068/1, EP/L017695/1 acknowledged by RF). SuperSTEM is the EPSRC National Facility for Advanced Electron Microscopy, supported by EPSRC. DTAR would like to acknowledge financial support provided by CONACyT. All research data supporting this publication are directly available within the publication.

REFERENCES

[1] R. Funahashi, I. Matsubara, S. Sodeoka, Thermoelectric properties of $Bi_2Sr_2Co_2O_x$ polycrystalline materials, Appl. Phys. Lett. 76 (2000) 2385–2387. doi:10.1063/1.126354.

[2] R. Funahashi, M. Shikano, $Bi_2Sr_2Co_2O_y$ whiskers with high thermoelectric figure of merit, Appl. Phys. Lett. 81 (2002) 1459–1461. doi:10.1063/1.1502190.

[3] D. Srivastava, F. Azough, R. Freer, E. Combe, R. Funahashi, D.M. Kepaptsoglou, Q.M. Ramasse, M. Molinari, S.R. Yeandel, J.D. Baran, S.C. Parker, Crystal structure and thermoelectric properties of Sr-Mo substituted $CaMnO_3$: a combined experimental and computational study, J. Mater. Chem. C. 3 (2015) 12245–12259. doi:10.1039/C5TC02318A.

[4] Y. Michiue, N. Kimizuka, Y. Kanke, Structure of $Ga_2O_3(ZnO)_6$: a member of the homologous series $Ga_2O_3(ZnO)_m$, Acta Crystallogr. Sect. B. 64 (2008) 521–526. https://doi.org/10.1107/S0108768108021125.

[5] Y. Michiue, N. Kimizuka, Superspace description of the homologous series $Ga_2O_3(ZnO)_m$, Acta Crystallogr. Sect. B. 66 (2010) 117–129. https://doi.org/10.1107/S0108768109053713.

[6] Y. Michiue, T. Mori, A. Prytuliak, Y. Matsushita, M. Tanaka, N. Kimizuka, Electrical, optical, and thermoelectric properties of $Ga_2O_3(ZnO)_9$, RSC Adv. 1 (2011) 1788–1793. doi:10.1039/C1RA00315A.

[7] Y. Michiue, N. Kimizuka, Y. Kanke, T. Mori, Structure of $(Ga_2O_3)_2(ZnO)_{13}$ and a unified description of the homologous series $(Ga_2O_3)_2(ZnO)_{2n+1}$, Acta Crystallogr. Sect. B. 68 (2012) 250–260. https://doi.org/10.1107/S0108768112016084.

[8] Y. Michiue, H. Nishijima, Y. Suzuki, T. Mori, Synthesis and thermoelectric properties of composite oxides in the pseudobinary system $ZnO\text{-}Ga_2O_3$, Solid State Sci. 65 (2017) 29–32. doi:https://doi.org/10.1016/j.solidstatesciences.2016.12.020.

[9] E. Guilmeau, P. Díaz-Chao, O.I. Lebedev, A. Rečnik, M.C. Schäfer, F. Delorme, F. Giovannelli, M. Košir, S. Bernik, Inversion Boundaries and Phonon Scattering in Ga:ZnO Thermoelectric Compounds, Inorg. Chem. 56 (2017) 480–487. doi:10.1021/acs.inorgchem.6b02354.

[10] M. Nakamura, N. Kimizuka, T. Mohri, The phase relations in the In_2O_3-Ga_2ZnO_4-ZnO system at 1350°C, J. Solid State Chem. 93 (1991) 298–315. doi:https://doi.org/10.1016/0022-4596(91)90304-Z.

[11] N. Kimizuka, M. Isobe, M. Nakamura, Syntheses and Single-Crystal Data of Homologous Compounds, $In_2O_3(ZnO)_m$ (m = 3, 4, and 5), $InGaO_3(ZnO)_3$, and $Ga_2O_3(ZnO)_m$ (m = 7, 8, 9, and 16) in the In_2O_3-$ZnGa_2O_4$-ZnO System, J. Solid State Chem. 116 (1995) 170–178. doi:https://doi.org/10.1006/jssc.1995.1198.

[12] M. Isobe, N. Kimizuka, M. Nakamura, T. Mohri, Structures of $LuFeO_3(ZnO)_m$ (m =1, 4, 5 and 6), Acta Crystallogr. Sect. C. 50 (1994) 332–336. https://doi.org/10.1107/S0108270193008108.

[13] C. Li, Y. Bando, M. Nakamura, K. Kurashima, N. Kimizuka, Structure analysis of new homologous compounds $Ga_2O_3(ZnO)_m$ (m = integer) by high-resolution analytical transmission electron microscopy, Acta Crystallogr. Sect. B. 55 (1999) 355–362. https://doi.org/10.1107/S0108768198018424.

[14] J.L.F. Da Silva, A. Walsh, S.-H. Wei, Theoretical investigation of atomic and electronic structures of $Ga_2O_3(ZnO)_6$, Phys. Rev. B. 80 (2009) 214118. https://link.aps.org/doi/10.1103/PhysRevB.80.214118.

[15] J. Barf, T. Walther, W. Mader, Twin Boundaries in Zinc Oxide with Additions of Gallium Oxide, Interface Sci. 12 (2004) 213–226. doi:10.1023/B:INTS.0000028651.74657.2b.

[16] J.-B. Labégorre, O.I. Lebedev, C. Bourgès, A. Rečnik, M. Košir, S. Bernik, A. Maignan, T. Le Mercier, L. Pautrot-d'Alençon, E. Guilmeau, Phonon Scattering and Electron Doping by 2D Structural Defects in In/ZnO, ACS Appl. Mater. Interfaces. (2018). doi:10.1021/acsami.7b19489.

[17] S.Isobe, and T.Tani, Y.Masuda, W.-S.Seo, K. Koumoto, Thermoelectric Performance of Yttrium-substituted $(ZnO)_5In_2O_3$ Improved through Ceramic Texturing, Jpn. J. Appl. Phys. 41 (2002) 731. http://stacks.iop.org/1347-4065/41/i=2R/a=731.

[18] Z. Xu, S. Ma, R. Chu, J. Hao, L. Cheng, G. Li, Low-temperature sintering of high potential gradient B_2O_3-doped ZnO varistors, J. Mater. Sci. Mater. Electron. 26 (2015) 4997–5000. doi:10.1007/s10854-015-3012-5.

[19] S.-W. Yoon, J.-H. Seo, T.-Y. Seong, T.H. Yu, Y.H. You, K.B. Lee, H. Kwon, J.-P. Ahn, Ga Ordering and Electrical Conductivity in Nanotwin and Superlattice-Structured Ga-Doped ZnO, Cryst. Growth Des. 12 (2012) 1167–1172. doi:10.1021/cg2010908.

[20] H. Rietveld, A profile refinement method for nuclear and magnetic structures, J. Appl. Crystallogr. 2 (1969) 65–71. https://doi.org/10.1107/S0021889869006558.

[21] A. Coelho, Topas Academic, (2014). http://www.topas-academic.net/.

[22] G. Lucas, P. Burdet, M. Cantoni, C. Hébert, Multivariate statistical analysis as a tool for the segmentation of 3D spectral data, Micron. 52–53 (2013) 49–56. doi:https://doi.org/10.1016/j.micron.2013.08.005.

[23] X. Liang, M. Baram, D.R. Clarke, Thermal (Kapitza) resistance of interfaces in compositional dependent ZnO-In_2O_3 superlattices, Appl. Phys. Lett. 102 (2013) 223903. doi:10.1063/1.4809784.

[24] X. Liang, D.R. Clarke, Relation between thermolectric properties and phase equilibria in the ZnO–In_2O_3 binary system, Acta Mater. 63 (2014) 191–201. doi:https://doi.org/10.1016/j.actamat.2013.10.027.

[25] M. Košir, M. Podlogar, N. Daneu, A. Rečnik, E. Guilmeau, S. Bernik, Phase formation, microstructure development and thermoelectric properties of $(ZnO)_kIn_2O_3$ ceramics, J. Eur. Ceram. Soc. 37 (2017) 2833–2842. doi:https://doi.org/10.1016/j.jeurceramsoc.2017.03.019.

[26] X. Liang, Thermoelectric transport properties of naturally nanostructured Ga–ZnO ceramics: Effect of point defect and interfaces, J. Eur. Ceram. Soc. 36 (2016) 1643–1650. doi:https://doi.org/10.1016/j.jeurceramsoc.2016.02.017.

Graphical Abstract (for review)

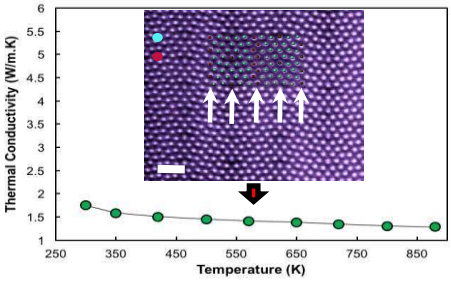

***Highlights (for review)**

Highlights

- High quality ceramic $Ga_2O_3(ZnO)_9$ has been synthesised
- Very low thermal conductivity for an oxide of 1.5 to 2.2 W/m.K has been achieved
- HAADF-STEM showed the presence of nano-sized, wedge-shaped twin boundaries
- The nano-scale features, chemically investigated for the first time, revealed the Zn and Ga distribution
- Ga ions occupy the sites at the interfaces of twin boundaries and inversion boundaries

Supplementary Material for on-line publication only

Click here to download Supplementary Material for on-line publication only: RF 17 May 18 Z9GO Supp JALCOM.docx